# Magneto-optical conductivity of a band-inverted charge transfer insulator

Chang Liu,[1] Sha-Sha Ke,[1] Yong Guo,[2] Xiao-Tao Zu,[1] Sean Li,[3] and Hai-Feng Lü[1,*]

[1]*School of Physics, University of Electronic Science and Technology of China, Chengdu 610054, China*

[2]*Department of Physics and State Key Laboratory of Low-Dimensional Quantum Physics, Tsinghua University, Beijing 100084, China*

[3]*School of Materials Science and Engineering, The University of New South Wales, Sydney, New South Wales 2052, Australia*

(Received 30 April 2024; accepted 10 July 2024; published 31 July 2024)

Recently, quantum anomalous Hall state has been observed in moiré transition metal dichalcogenide bilayers. Its topological physics can be explained by a band-inverted charge transfer insulator model, in which the topological phase transition occurs in the presence of the band inversion. Starting from an effective three-band low-energy model, we investigate the Landau levels and the magneto-optical conductivity of a band-inverted charge transfer insulator on the honeycomb lattice. We derive the real and imaginary parts of the longitudinal conductivity and Hall conductivity using Kubo formalism. We find that the magneto-optical conductivity indicates a discontinuity at the point of band inversion in the low-frequency regime, which can serve as a probe for band topology. It is shown that the charge transfer gap, chemical potential, and magnetic field have a sensitive effect on the magneto-optical conductivity. The unique band structure also changes the peaks in the imaginary part of the Hall conductivity into two distinct contributions of opposite signs. We also study the relationship of the band-inversion signature and transport properties and highlight its distinct features that can be probed experimentally.

DOI: 10.1103/PhysRevB.110.045445

## I. INTRODUCTION

When a material is subjected to an external magnetic field, the electron energy spectrum is usually quantified as discrete Landau levels (LLs). Magneto-optical conductivity spectrum originates from the optical transitions between these discrete LLs [1–3]. As the LLs directly related to the nature of the system, magneto-optical conductivity is a crucial and practical technique for detection of target material's electronic properties [4–10]. For instance, information such as the energy gap, the characteristics of the band structure, and the Fermi velocity of systems can be extracted from the resonant peaks of optical conductivity. The optical spectrum shows information in the positions and heights of peaks as well as in the shift of the peaks due to variations of system parameters such as magnetic field and chemical potential. Especially, the magneto-optical property can be also served as a sensitive experimental method to detect the inner topologies [11–13].

In recent years, the LL formation and characteristics of Dirac materials like two-dimensional (2D) materials [14–24] and topological insulators [12,25–28] under an external magnetic field have been widely investigated. It is found that the energy dispersion of LLs in monolayer graphene is proportional to $\sqrt{nB}$, where $n$ denotes LL index and $B$ stands for the magnetic field [14]. The conduction and valence bands in graphene are mirror symmetric, with the $n = 0$ flat band residing at zero energy. Additionally, the related research has also been extended to multilayer graphene [17,20,21]. The magneto-optical conductivity of 2D Dirac materials like graphene and the surface state of three-dimensional (3D) topological insulator exhibits a set of asymmetric peaks situated above a flat background [14,19,20,27,29]. For Weyl semimetals, they produce a set of asymmetric peaks on a linear background [15,22]. In the presence of a quadratic momentum factor in the low-energy Hamiltonian, it is found that the LLs spacings are proportional to the magnetic field $B$ and drastically different from the square root of $B$ law [22,27]. This has important implications for the optical absorption. The quadratic momentum term breaks the particle-hole symmetry and splits the magneto-optical absorption line into two peaks structure [22,27].

For the one-band Hubbard models with half-filling, a large enough Coulomb repulsion can suppress double occupancy per unit and produce the Mott insulating state [30–36]. In a Mott insulator, the mutual Coulomb repulsion prevents the conduction electrons from moving and their strong electron correlation keeps them entirely isolated on their respective atomic sites. The charge transfer insulators can be categorized within the broader Mott insulator framework [37–40]. In a charge transfer insulator, the energy cost is less than the Coulomb interaction when transferring an electron between the anion and the cation without creating double occupancy. The physics of charge transfer insulators is captured by a two-band Hubbard model, where the band derived from anions is located inside the Mott gap of the cation states. A typical energy gap in a charge transfer insulator is formed between the unoccupied (upper) $d$-electron Hubbard band and the occupied chalcogen (like oxygen) $p$-electron band.

A physical realization of charge transfer insulators with highly controllable gap by a displacement field could be realized in moiré transition metal dichalcogenide bilayers

*Contact author: lvhf04@uestc.edu.cn

 ©2024 American Physical Society

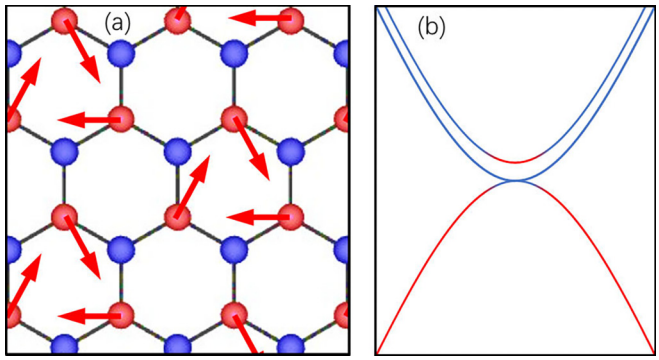


FIG. 1. (a) A schematic sketch of the real-space structure of the $MoTe_2/WSe_2$ bilayer illustrating the honeycomb moiré lattice. Red and blue dots denote the $A$ and $B$ sublattices, respectively. Red arrows represent $2\pi/3$ $xy$ antiferromagnetic order on the $A$ sublattice. (b) The inverted band structure of the effective three-band Hamiltonian, showing a quadratic band touching. The $A$ band is above the $B$ bands after the twofold degeneracy $B$ band dips below it.

[41–49]. Recently, quantum anomalous Hall effect has been observed in $AB$-stacked $MoTe_2/WSe_2$ moiré heterobilayers experimentally [50,51]. The appearance of the topological phase can be described by a band-inverted charge transfer insulator mechanism based on a two-band Hubbard model [52]. It has been identified that a quadratic band-touching point has topological feature, and can be driven towards a quantum anomalous Hall phase with time-reversal symmetry breaking even under arbitrary weak interactions, while strong interactions may lead to other competing phases [53,54].

The band inversion between cation and anion bands in a charge transfer insulator induces a transition from a Mott insulator to a topologically nontrivial state. Therefore, it is important to detect the nature of the gap related to the competition between charge transfer energy and Coulomb repulsion. In this work, we present a systematic investigation of the magneto-optical response of the charge transfer insulators with both linear and quadratic energy terms, based on the low-energy effective Hamiltonian and Kubo formula. It is expected that the information about the charge transfer gap, LLs properties, and band-inversion signature could be extracted from the magneto-optical conductivity.

This paper is organized as follows. In Sec. II, we present the effective low-energy Hamiltonian and compute the LLs analytically. We also discuss the effects of the magnetic field on the LLs and how the LL spectra vary when tuning the charge transfer gap. In Sec. III, we calculate the magneto-optical conductivity and discuss the selection rules of the optical absorption between different LLs. We also investigate the effect of the charge transfer gap and the chemical potential on the transport properties. In Sec. IV, we finally give a summary of our findings.

## II. LANDAU-LEVEL SPECTRUM

We start our discussion from a low-energy effective Hamiltonian of a band-inverted charge transfer insulator first [52]. Especially, the charge transfer model considered here is resemble to the 2D moiré superlattices in semiconductor heterostructures. The model has been used to describe the phase transition from a correlated insulator to a quantum anomalous Hall state in $AB$-stacked $MoTe_2/WSe_2$ heterostructures. The model Hamiltonian we considered here is given by

$$\mathcal{H} = \begin{pmatrix} -\frac{k^2}{2m_A} & \lambda k_- & -\lambda e^{i\theta} k_+ \\ \lambda k_+ & \frac{k^2}{2m_B} + \delta & 0 \\ -\lambda e^{-i\theta} k_- & 0 & \frac{k^2}{2m_B} + \delta \end{pmatrix}, \tag{1}$$

where $e^{i\theta}$ represents the in-plane order on the $A$ sublattice and $\lambda$ is a dimensionless parameter modeling the effective mass and spin-orbit coupling. $k_\pm = k_x \pm ik_y$, and the charge transfer gap is denoted by $\delta$. The $A$ and $B$ sublattices represent the cation and anion, and the effective masses are given by $m_A$ and $m_B$, respectively. The other $A$ band is ignored as it is far from the Fermi level due to the different influence of the Coulomb repulsion. It is noted that we do not start from an interacting Hubbard-type model, and the effective low-energy model is taken into account. Actually, the interaction term $gn_{B\uparrow}n_{B\downarrow}$ on the anions plays an essential role after the charge transfer gap is inverted. The spin-degenerate model of $B$ sublattice with an interaction term $gn_{B\uparrow}n_{B\downarrow}$ has been considered by performing the Hartree-Fock treatment and density matrix renormalization group calculations [52]. The results indicate that in the presence of even arbitrarily weak repulsive interactions, the quadratic band touching is unstable and towards the opening of a topological gap, resulting in a quantum anomalous Hall state.

Here electrons in the charge transfer band are spin degenerate prior to the inversion, whereas holes connected to the lower Hubbard band are spin nondegenerate. Band inversion across bands can be induced by further reducing the charge transfer energy to invert the charge transfer gap. Following this transition, an insulating state can be thought of as having a negative charge transfer gap, similar to the negative band gap found in inverted semiconductors. As a result, quantum anomalous Hall state arises after inverting the charge transfer gap [55–58]. The quadratic momentum term and the negative charge transfer gap term lead to a quadratic band-touching structure in band structure, as shown in Fig. 1.

In the presence of a magnetic field, the continuous bands become quantized into discrete LLs. To get the LL spectrum of the Hamiltonian, we start with a uniform magnetic field along the $z$ direction, and in this case the LL spectrum can be analytically obtained. The applied magnetic field quantizes the motion of the electrons in the $x$-$y$ plane. We make the Peierls substitution $k \Rightarrow \Pi = k + A$ for describing tightly bound electrons in the magnetic field and choose the Landau gauge. Correspondingly, the vector potential in the effective Hamiltonian is chosen as $A = (0, Bx, 0)$. We ignore the Zeeman effect caused by magnetic fields in our calculations for simplicity. By introducing the creation and annihilation operators $a^\dagger = \frac{l_B}{\sqrt{2}}(\Pi_x + i\Pi_y)$, $a = \frac{l_B}{\sqrt{2}}(\Pi_x - i\Pi_y)$, the effective

Hamiltonian can be written as

$$\mathcal{H} = \begin{pmatrix} -\frac{1}{m_A {l_B}^2}(a^\dagger a + 1/2) & \frac{\sqrt{2}\lambda}{l_B} a & -\frac{\sqrt{2}\lambda}{l_B} e^{i\theta} a^\dagger \\ \frac{\sqrt{2}\lambda}{l_B} a^\dagger & \frac{1}{m_B {l_B}^2}(a^\dagger a + 1/2) + \delta & 0 \\ -\frac{\sqrt{2}\lambda}{l_B} e^{-i\theta} a & 0 & \frac{1}{m_B {l_B}^2}(a^\dagger a + 1/2) + \delta \end{pmatrix}, \tag{2}$$

where $l_B = \sqrt{\hbar/(eB)}$ denotes the magnetic length and the creation and annihilation operators satisfy the commutation rule $[a, a^\dagger] = 1$.

We can solve $H\Psi = E\Psi$ by setting $\Psi = (\chi_1|n\rangle, \chi_2|n+1\rangle, \chi_3|n-1\rangle)^T$. Within a same band, each LL is indexed by the Fock number $n$. The eigenstates are a mixture of spin down of $A$ for $|n\rangle_\uparrow$, spin up of $B$ for $|n+1\rangle_\uparrow$, and spin down of $B$ for $|n-1\rangle_\downarrow$. The corresponding eigenequation is given by

$$\begin{pmatrix} -\frac{1}{m_A {l_B}^2}(n + 1/2) - E & \frac{\sqrt{2}\lambda}{l_B}\sqrt{n+1} & -\frac{\sqrt{2}\lambda}{l_B} e^{i\theta}\sqrt{n} \\ \frac{\sqrt{2}\lambda}{l_B}\sqrt{n+1} & \frac{1}{m_B {l_B}^2}(n + 3/2) + \delta - E & 0 \\ -\frac{\sqrt{2}\lambda}{l_B} e^{-i\theta}\sqrt{n} & 0 & \frac{1}{m_B {l_B}^2}(n - 1/2) + \delta - E \end{pmatrix} \begin{pmatrix} \chi_1 \\ \chi_2 \\ \chi_3 \end{pmatrix} = 0. \tag{3}$$

To obtain nontrivial solution of the eigenvectors, it requires $\mathrm{Det}(H - E) = 0$. Setting $A = -\frac{1}{m_A {l_B}^2}(n + \frac{1}{2})$, $B_1 = \frac{1}{m_B {l_B}^2}(n + \frac{3}{2}) + \delta$, and $B_2 = \frac{1}{m_B {l_B}^2}(n - \frac{1}{2}) + \delta$, the equation of the LL spectrum is deduced as

$$\frac{2\lambda^2}{l_B^2}[n(B_1 - E) + (n+1)(B_2 - E)] - (B_1 - E)(B_2 - E)(A - E) = 0. \tag{4}$$

The roots of the cubic polynomial equation can be solved analytically via Cardano's formula. The eigenvalues and eigenstates of the matrix can be obtained analytically and numerically. The components of the wave function are also thus obtained. Although the analytic forms for the LL spectra are rather complex, the approximated analytical expression of LLs could be obtained in the case of $n \gg 1$. In this case, $B_1 \approx B_2 \approx n/(m_B {l_B}^2) + \delta$ and three LL branches can be approximately expressed as

$$\begin{aligned} E_{n\gg 1,\pm} &\approx \frac{n}{2l_B^2}\left(\frac{1}{m_B} - \frac{1}{m_A}\right) + \frac{\delta}{2} \\ &\quad \pm \sqrt{\left[\frac{n}{2l_B^2}\left(\frac{1}{m_B} + \frac{1}{m_A}\right) + \frac{\delta}{2}\right]^2 + \frac{16n\lambda^2}{l_B^2}}, \\ E_{n\gg 1,0} &\approx \frac{n}{m_B {l_B}^2} + \delta. \end{aligned} \tag{5}$$

For the relatively weak magnetic field, it can be deduced that two LL branches $E_{n\gg 1,\pm}$ indicate $\sqrt{nB}$ dependence on the magnetic field and they are separated by an energy gap $\delta$ approximately. Differently, the third LL branch $E_{n\gg 1,0}$ shows a linear-$B$ dependence as $E_{n\gg 1,0} \propto nB$.

In the opposite case of the lowest LL $n = 0$, the eigenequation is given by

$$\begin{pmatrix} -\frac{1}{2m_A {l_B}^2} - E & \frac{\sqrt{2}\lambda}{l_B} & 0 \\ \frac{\sqrt{2}\lambda}{l_B} & \frac{3}{2m_B {l_B}^2} + \delta - E & 0 \\ 0 & 0 & 0 \end{pmatrix} \begin{pmatrix} \chi_1 \\ \chi_2 \\ 0 \end{pmatrix} = 0 \tag{6}$$

and the LL for $n = 0$ can be simply solved as

$$\begin{aligned} E_{0\pm} &= \frac{1}{4l_B^2}\left(\frac{3}{m_B} - \frac{1}{m_A}\right) + \frac{\delta}{2} \\ &\quad \pm \sqrt{\left[\frac{1}{4l_B^2}\left(\frac{3}{m_B} + \frac{1}{m_A}\right) + \frac{\delta}{2}\right]^2 + \frac{8\lambda^2}{l_B^2}}. \end{aligned} \tag{7}$$

In the calculation, we take $m_A = 0.35m_e$ and $m_B = 0.65m_e$ [41,49–51] from the experimentally determined values of $AB$-stacked $MoTe_2/WSe_2$ heterostructures for calculating, where $m_e$ is the bare electron mass. Other system parameters are taken as $\theta = \frac{2\pi}{3}$ [52] and $\lambda = 0.1$.

In Fig. 2, we present the evolution of the LL energy spectrum as a function of the magnetic field for different charge transfer gap values. The four lowest LLs indexed by $n = 0$ (black lines), $n = 1$ (red lines), $n = 2$ (blue lines), and $n = 3$ (green lines) are depicted to show the effect of charge transfer energy and magnetic field. It is shown in Fig. 2 that there are two types of LL branches for $n > 1$ in the low magnetic field regime: one branch exhibiting linear dependence on the magnetic field $B$ and two branches showing the $\sqrt{B}$ dependency. Here, the lowest LL with index $n = 0$ belongs to the second type of branches. With the increase of the magnetic field, the LLs crossing appears between the LL branch with $\sqrt{B}$ dependence and the branch with linear dependence on $B$. It is noted that for strong magnetic field, the positive $\sqrt{B}$-resolved LL branch with index $n$ is gradually equal with the linear-$B$-dependent branch with $n + 2$. Furthermore, the $\sqrt{B}$-resolved branches do not exhibit mirror symmetry. Consequently, the absorption peaks in magneto-optical conductivity could reflect the imperfect mirror symmetry between the positive and negative branches of the LL spectrum.

In the limit of weak magnetic field $B = 0$, it can be deduced from Eq. (7) that the eigenstates are highly degenerate with $E = 0, \delta$. The LL spectra are separated by the energy gap $\delta$. As shown in Fig. 2, the linear-$B$-dependent branch of the system is pinned at different points in the conduction and valence bands in different signs of charge energy gap $\delta$. In the case of $\delta > 0$, the linear-$B$-dependent LL branch is always

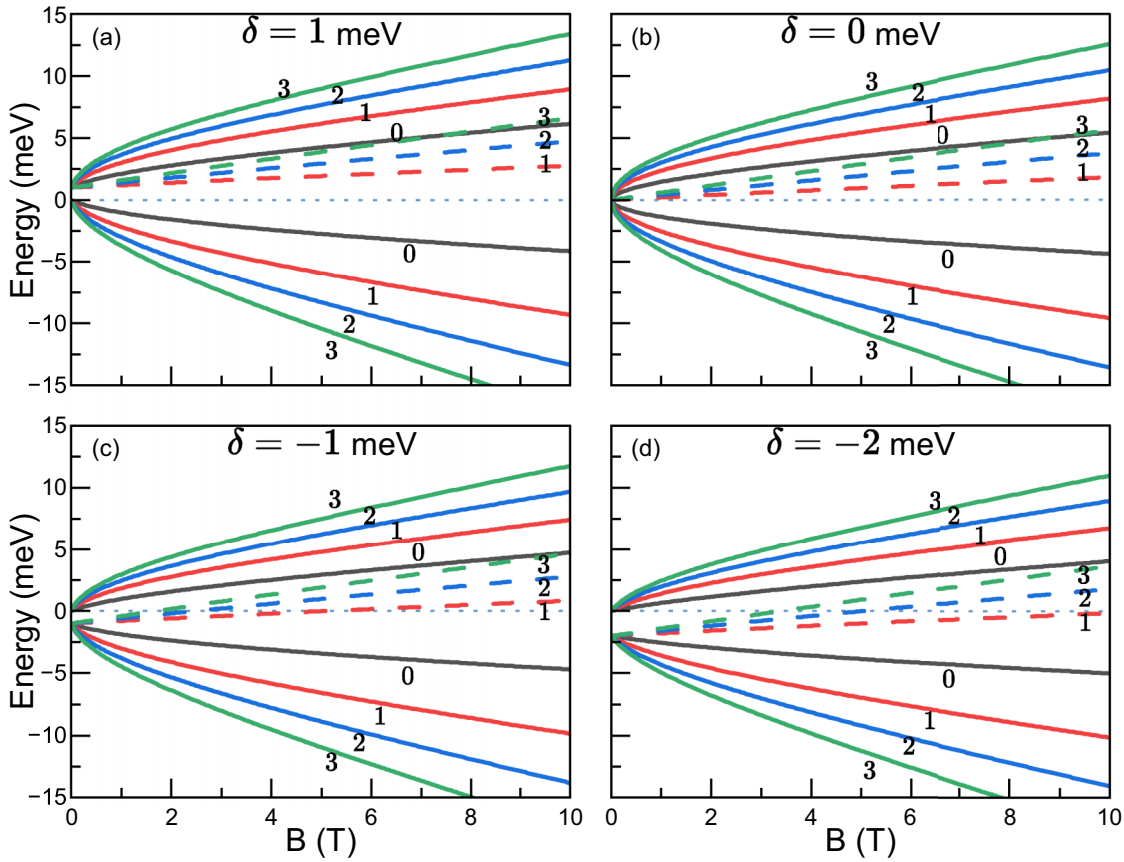


FIG. 2. The lowest four sets of Landau levels as a function of the magnetic field $B$ for different charge transfer gaps (a) $\delta = 1$ meV, (b) $\delta = 0$ meV, (c) $\delta = -2$ meV, and (d) $\delta = -1$ meV. The LL indices are indicated by different line colors: $n = 0$ (black lines), $n = 1$ (red lines), $n = 2$ (blue lines), and $n = 3$ (green lines). The blue gray dotted line is the zero-energy line.

located in the conduction band as a function of the magnetic field. In the case of $\delta = 0$, the charge transfer gap between different bands closes and the linear-$B$-dependent LL branch starts from zero energy. As $\delta$ decreases further and becomes negative, the energy gap reopens and the system undergoes a band-inverted phase transition. The location of the linear-$B$-dependent LL branch shifts to the valence band with the decrease of $\delta$ and the linear-$B$-dependent branch crosses zero energy at a critical magnetic field, as shown in Figs. 2(c) and 2(d).

Here the band gap in our model is inverted by the negative charge transfer gap, the sign reversal of the band gap is related to the LL crossing or pinned at these points. Actually, this signature of LLs has also been shown in several other topological systems and been suggested to detect the topological nature of electronic bands [11–13,59,60]. For instance, in inverted HgTe quantum wells, it is known that the lowest conduction LL and the uppermost valence LL cross at a finite critical magnetic field [11,59–61]. In a Floquet topological insulator thin film, it is shown that the electrons of the top and bottom surface states are pinned at different points in the $n = 0$ LLs for different topological phases [12]. The features of LLs are also suggested to serve as a probe for band topology in moiré superlattice systems characterized by bands with nontrivial valley Chern numbers [13].

We then study the influence of the charge transfer gap $\delta$. Figure 3 illustrates the lowest 11 LLs as a function of charge transfer gap with different magnetic fields. It is shown that two LL branches are always positive or negative and one branch undergoes the sign reversal as a function of the gap $\delta$. The positive LL branch and the negative one are separated by an energy gap, which is determined by the charge transfer gap and the magnetic field. In the low magnetic field limit, the linear-$B$-resolved LL branch is highly degenerate. In the case of $\delta < 0$, it implies that numerous electronic states are occupied in a small energy range, which is similar to a nearly flat band. Therefore, it is expected that the interaction and correlation between electrons becomes important in this system. With the increase of the magnetic field, the energy splitting of LLs is strongly enhanced. These features of LLs can sensitively affect the optical absorption and magneto-optical conductivity properties, as we discuss later.

## III. MAGNETO-OPTICAL CONDUCTIVITY

In this section, we study the magneto-optical conductivity of the band-inverted charge transfer insulator with different charge transfer gaps and chemical potentials. The LL spectrum reflects the band-inversion signature, as demonstrated above; it is thus expected that such a feature leads to a

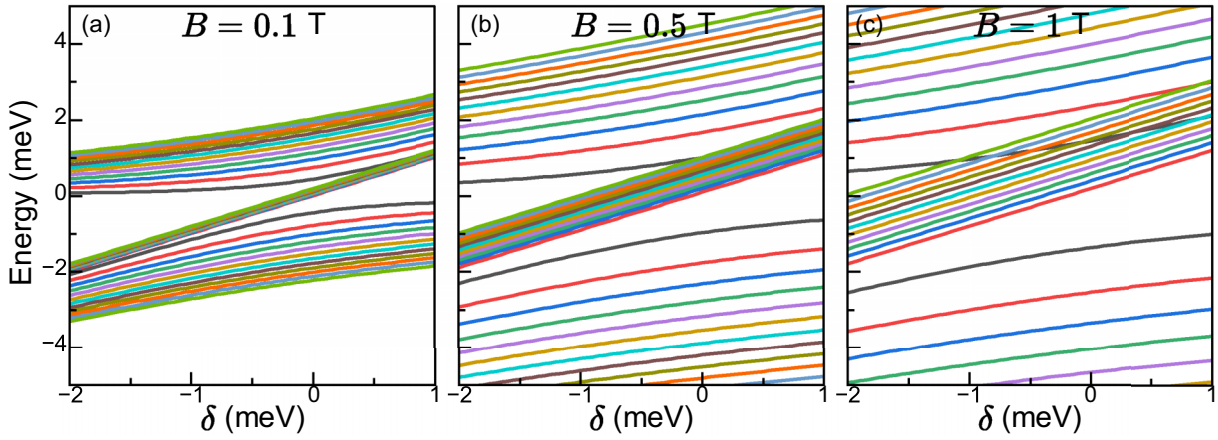


FIG. 3. Landau-level spectrum of $n < 12$ as a function of the charge transfer gap $\delta$ for different magnetic fields (a) $B = 0.1$ T, (b) $B = 0.5$ T, and (c) $B = 1$ T. The LL indices are indicated by different line colors.

significant change in the magneto-optical conductivity image. The critical magnetic field for the sign reversal of the linear-$B$-dependent LL branch is also expected to be extracted from the magneto-optical conductance. With the knowledge of the LLs and eigenvectors of the Hamiltonian under a magnetic field, the magneto-optical conductivity can be obtained from the Kubo formula [62,63]. The standard Kubo formalism is utilized to derive the expressions for the magneto-optical conductance by taking into account the optical, magnetic fields, and frequency dependence. Expressed in the LL basis in the clean limit, the general expression of the Kubo formula is as follows:

$$\sigma_{\alpha\beta} = -\frac{i\hbar e^2}{2\pi l_B^2}\sum_{nn'}\sum_{ii'}\left[\frac{f(E_{ni}) - f(E_{n'i'})}{E_{ns} - E_{n'i'}}\right] \times \frac{\langle\psi_{n,i}|j_\alpha|\psi_{n',i'}\rangle\langle\psi_{n',i'}|j_\beta|\psi_{n,i}\rangle}{\omega + E_{ni} - E_{n'i'} + i\epsilon}, \tag{8}$$

where $f(x) = 1/[1 + e^{\beta(x-\mu)}]$ denotes the Fermi-Dirac distribution function, $\beta$ is the inverse temperature, and $\mu$ is the chemical potential. The current density operators are given by $j_\alpha = i[\mathcal{H}, x_\alpha] = \frac{\partial\mathcal{H}}{\partial\Pi_\alpha}$ with

$$j_x = \begin{pmatrix} -\frac{1}{m_A}\Pi_x & \lambda & -\lambda e^{i\theta} \\ \lambda & \frac{1}{m_B}\Pi_x & 0 \\ -\lambda e^{-i\theta} & 0 & \frac{1}{m_B}\Pi_x \end{pmatrix},$$

$$j_y = \begin{pmatrix} -\frac{1}{m_A}\Pi_y & -i\lambda & -i\lambda e^{i\theta} \\ i\lambda & \frac{1}{m_B}\Pi_y & 0 \\ i\lambda e^{-i\theta} & 0 & \frac{1}{m_B}\Pi_y \end{pmatrix}. \tag{9}$$

The matrix elements of the current density operators can be calculated by dividing them into diagonal and off-diagonal parts. Replacing $\Pi_\alpha$ with $a$ and $a^\dagger$, the overlapping matrix elements $\langle\psi_{n,i}|j_\alpha|\psi_{n',i'}\rangle$ can be directly evaluated and its detail derivation process is given in the Appendix. Substituting the expression of current operators into the Kubo equation, the dissipative components corresponding to the absorptive parts of the longitudinal conductivity tensor $\sigma_{xx}$ and the transverse Hall conductivity tensor $\sigma_{xy}$ can be obtained as

$$\sigma_{xx} = -\frac{i\hbar e^2}{2\pi l_B^2}\sum_{ii'}\left[\frac{f(E_{0i}) - f(E_{1i'})}{E_{0i} - E_{1i'}}\frac{M_{x,0i}^{1i'}M_{x,1i'}^{0i}}{\omega + E_{0i} - E_{1i'} + i0^+} + \sum_{n=1}\left(\frac{f(E_{ni}) - f(E_{n+1i'})}{E_{ni} - E_{n+1i'}}\frac{M_{x,ni}^{n+1i'}M_{x,n+1i'}^{ni}}{\omega + E_{ni} - E_{n+1i'} + i0^+} + \frac{f(E_{ni}) - f(E_{n-1i'})}{E_{ni} - E_{n-1i'}}\frac{M_{x,ni}^{n-1i'}M_{x,n-1i'}^{ni}}{\omega + E_{ni} - E_{n-1i'} + i0^+}\right)\right] \tag{10}$$

and

$$\sigma_{xy} = -\frac{i\hbar e^2}{2\pi l_B^2}\sum_{ii'}\left[\frac{f(E_{0i}) - f(E_{1i'})}{E_{0i} - E_{1i'}}\frac{M_{x,0i}^{1i'}M_{y,1i'}^{0i}}{\omega + E_{0i} - E_{1i'} + i0^+} + \sum_{n=1}\left(\frac{f(E_{ni}) - f(E_{n+1i'})}{E_{ni} - E_{n+1i'}}\frac{M_{x,ni}^{n+1i'}M_{y,n+1i'}^{ni}}{\omega + E_{ni} - E_{n+1i'} + i0^+} + \frac{f(E_{ni}) - f(E_{n-1i'})}{E_{ni} - E_{n-1i'}}\frac{M_{x,ni}^{n-1i'}M_{y,n-1i'}^{ni}}{\omega + E_{ni} - E_{n-1i'} + i0^+}\right)\right]. \tag{11}$$

Here $M_{x,ni}^{n'i'} = \langle\psi_{n,i}|j_x|\psi_{n',i'}\rangle$ and $M_{y,ni}^{n'i'} = \langle\psi_{n,i}|j_y|\psi_{n',i'}\rangle$ denote the transition rates between different LLs and their expression is given in the Appendix. The first term in the magneto-optical conductivity means the contribution related to the LL with $n = 0$, which is considered separately.

Optically allowed interband and intraband LL optical transitions should satisfy the selection rule of $n' = n \pm 1$. Transition between the same LL branch with different index $n$ is called intraband transition, and the interband transition represents the optical absorption between different LL branches. Through the absorption of the photon with certain frequency, one electron could be excited from the valence band to the unoccupied states and the magneto-optical conductance is thus generated. For convenience, the three LL branches are labeled by $L_T$, $L_M$, and $L_B$, respectively. Here $L_T$ and $L_B$

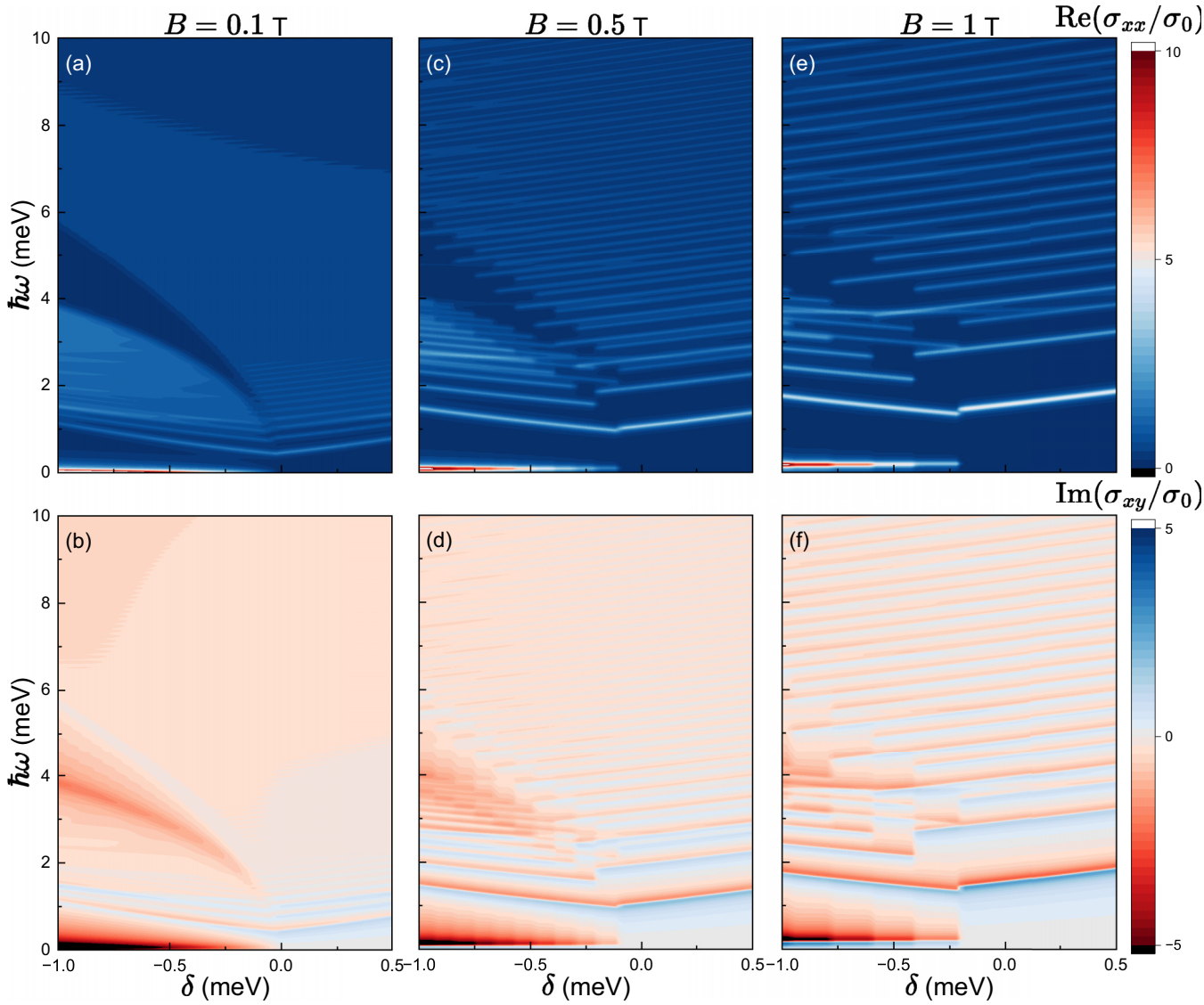


FIG. 4. (a), (c), (e) The real part of the longitudinal optical conductivity $\mathrm{Re}(\sigma_{xx})$ and (b), (d), (f) the imaginary part of the transverse Hall conductivity $\mathrm{Im}(\sigma_{xy})$ plotted as a function of the charge transfer gap $\delta$ in units of $\sigma_0 = \frac{\hbar e^2}{2\pi l_B^2}$ for different magnetic fields $B = 0.1$, 0.5, and 1 T (from left to right), respectively. Other parameters are taken as the chemical potential $\mu = 0$ meV and the temperature $T = 0.05$ K.

represent the positive and negative $\sqrt{B}$-resolved LL branches, while $L_M$ denotes the linear-$B$-dependent branch. We use the notation $T_{ni}^{mj}$ to denote transitions originating from a LL with index $n, i$ to the LL with index $m, j$, where $i, j$ stand for the index of the three bands. In the calculation, we take the low temperature $T = 0.05$ K, the chemical potential $\mu = 0$ meV, and $\epsilon = 0.05$ meV to discuss the longitudinal magneto-optical conductivity $\sigma_{xx}$ and the transverse Hall conductivity $\sigma_{xy}$. Furthermore, $\sigma_0 = \frac{\hbar e^2}{2\pi l_B^2}$ is taken as the unit of conductance.

### A. Influence of charge transfer gap and magnetic field

We first consider the effect of the charge transfer gap $\delta$ on the magneto-optical conductance. The real part of the longitudinal $\mathrm{Re}(\sigma_{xx})$ and imaginary parts of the transverse Hall conductivity $\mathrm{Im}(\sigma_{xy})$ are demonstrated in Fig. 4 as functions of photonic energies and charge transfer gap for different magnetic fields. As illustrated in Fig. 4, the conductance peaks indicate the linear dependence on the charge transfer gap $\delta$. It is noted that the conductance peaks show discontinuity points when the band inversion occurs near the band inversion of $\delta = 0$, especially for low magnetic fields and low photonic energies. These points shift towards lower $\delta$ with the increase of photon energy and magnetic field. The interval between the conductance peaks becomes wider with the decrease of $\delta$. For the negative charge transfer gap $\delta < 0$, an extra conductance peak is induced at low photonic energy, while it is absent for $\delta > 0$. The extra conductance peak origins from optical absorption between the electrons of the linear-$B$-resolved LL branch. Therefore, these features in the magneto-optical conductance could serve as a signature of the band inversion and related topological phase transition. With the increase of the magnetic field $B$, the discontinuity point of the conductance peaks moves towards to the higher photonic energy regime.

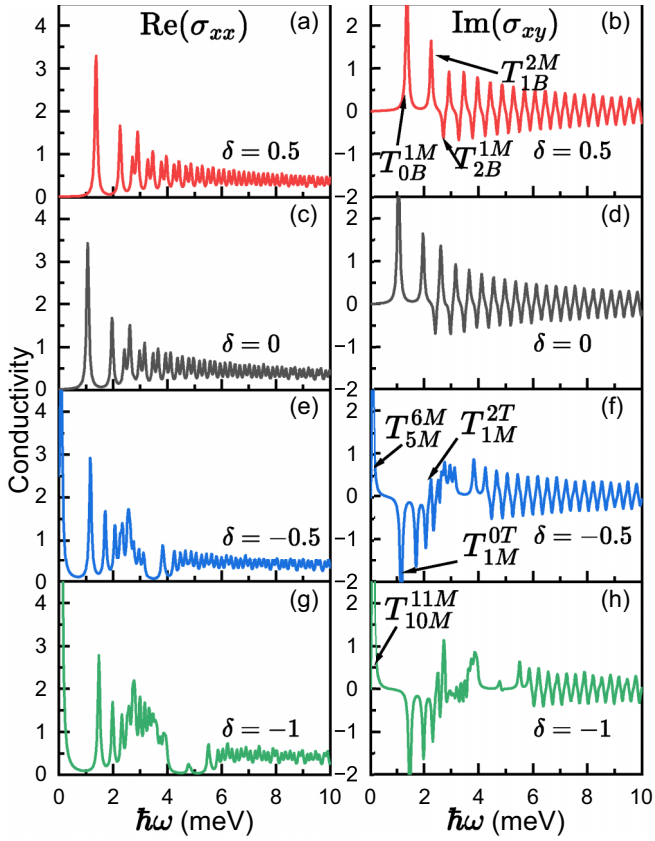


FIG. 5. The real part of longitudinal magneto-optical conductivity $\mathrm{Re}(\sigma_{xx})$ and the imaginary part of transverse Hall conductivity $\mathrm{Im}(\sigma_{xy})$ versus the photon energy $\hbar\omega$ for different charge transfer gaps $\delta = 0.5$ meV in (a) and (b), 0 meV in (c) and (d), $-0.5$ meV in (e) and (f), and $-1$ meV in (g) and (h), respectively. Other parameters are taken as the magnetic field $B = 0.5$ T and the chemical potential $\mu = 0$ meV and the conductance is in units of $\sigma_0 = \frac{\hbar e^2}{2\pi l_B^2}$.

In Fig. 5 we present the magneto-optical conductance $\mathrm{Re}(\sigma_{xx})$ and $\mathrm{Im}(\sigma_{xy})$ as a function of photon energy for different charge transfer gaps $\delta$. It can be deduced from Eq. (11) that the transitions $n+1 \to n$ lead to negative peaks in the imaginary Hall conductivity. As illustrated in Fig. 5, transitions of electrons between different LLs produce a series of absorption resonance peaks against a flat background, similar to the the magneto-optical conductance in graphene [14,29]. With the decrease of the charge transfer gap $\delta$, most conductance peaks gradually shift towards lower magnetoexcitation frequencies with increased spectral heights.

We initially concentrate on the case of $\delta \geqslant 0$. In this case the interband transitions satisfy the selection rule and make the predominant contribution to magneto-optical conductivity at low-frequency regime. The first two positive peaks on the left side are from the transitions $T_{0B}^{1M}$ and $T_{1B}^{2M}$, and the first negative peak is origin from $T_{2B}^{1M}$. Interestingly, the transitions $T_{2B}^{3M}$ and $T_{1B}^{0T}$ have the similar transition energy lengths, resulting in their combined contribution to the formation of the third positive peak. However, the contribution of the transition $T_{1B}^{0T}$ is relatively small. A similar transition rule governs the occurrence of other peaks at higher magnetoexcitation energies, expressed as $T_{pB}^{(p+1)M}$, $T_{pB}^{(p-1)M}$, $T_{pB}^{(p-1)T}$, $T_{pB}^{(p+1)T}$. Among these transitions, $T_{pB}^{(p-1)M}$ manifests as a negative peak with an intensity comparable to the positive peak from $T_{pB}^{(p+1)M}$ with similar transition energies. Due to the larger transition energy of $T_{(p-1)B}^{pT}$ and $T_{pB}^{(p-1)T}$, the corresponding peak is smaller and located at a higher photon energy. Similar with the peaks generated from $T_{pB}^{(p+1)M}$ and $T_{pB}^{(p-1)M}$, the peaks origin from $T_{(p-1)B}^{pT}$ and $T_{pB}^{(p-1)T}$ does not merge into one peak due to imperfect mirror symmetry between the positive and negative LL branches.

However, the magneto-optical conductivity is quite different in the band-inverted case of $\delta < 0$. In this case, the conductance peak contributed by the competition between the transitions $T_{1M}^{0T}$ and $T_{0B}^{1M}$ becomes negative. Importantly, the conductance peak close to the low-frequency limit $\hbar\omega = 0$ appears, which is mainly contributed by the intraband transitions $T_{pM}^{(p+1)M}$. For the band-inverted case, the conductance peaks induced by the transitions $T_{pM}^{(p+1)M}$, $T_{pM}^{(p-1)T}$, and $T_{pM}^{(p+1)T}$ begin to appear, while they are absent for $\delta > 0$. The appearance of these new transitions is contributed by the linear-$B$-resolved LL branch $L_M$ with its energy below the chemical potential. It is shown in Fig. 5 that there is an energy interval when $\delta < -0.5$ meV where only some small peaks are resident in. The energy range of the interval is decided by how many transitions of $T_{pB}^{(p+1)M}$ and $T_{pB}^{(p-1)M}$ are blocked. The small peaks in this region are induced by the transitions from the LL branch $L_B$ to $L_T$, which are ignorable before.

At the band-inversion point $\delta = 0$, it is shown in Fig. 5 that the sign of the conductivity peaks in $\mathrm{Im}(\sigma_{xy})$ switches, as a result of the band-gap closure. With the decrease of $\delta$, the optical absorption caused by the transition $T_{0B}^{1M}$ moves to the lower energy, while the peak induced by $T_{1M}^{0T}$ moves to the higher-energy regime. The competition between these two transitions leads to the discontinuity near the band-inversion point $\delta = 0$ in both $\mathrm{Re}(\sigma_{xx})$ and $\mathrm{Im}(\sigma_{xy})$, as illustrated in Fig. 4. Furthermore, it is also shown in Fig. 5 that the peak of the conductance $\mathrm{Re}(\sigma_{xx})$ and $\mathrm{Im}(\sigma_{xy})$ near the low-frequency limit $\hbar\omega = 0$ appears only in the band-inverted case. The magneto-optical conductance peak in the low-frequency regime manifests the closing and reopening signature of the charge transfer gap.

In the following, we turn to discuss the magneto-optical conductivity under circularly polarized light. From the longitudinal conductivity $\sigma_{xx}$ and the transverse Hall conductivity $\sigma_{xy}$, one can define the polarized conductance $\sigma_\pm = \sigma_{xx} \pm i\sigma_{xy}$ with the right-handed polarization conductance $\sigma_+$ and left-handed polarization part $\sigma_-$, respectively. The polarized conductance $\mathrm{Re}(\sigma_\pm) = \mathrm{Re}(\sigma_{xx}) \mp \mathrm{Im}(\sigma_{xy})$ is demonstrated in Fig. 6. Correspondingly, the heights of the original positive peaks in $\mathrm{Im}(\sigma_{xy})$ are doubled in $\mathrm{Re}(\sigma_-)$ while the negative part is diminished. We focus on the $\mathrm{Re}(\sigma_+)$ as it directly gives the differences between the longitudinal and Hall conductivity. As mentioned before, the peaks at higher energies are little affected by varying the system parameters. Interestingly, the right circular polarization conductivity $\sigma_+$ exhibits a series of peaks at low-frequency regime for the band-inverted case of $\delta < 0$, which origins from the transitions $T_{pM}^{(p-1)T}$. And the interval in $\mathrm{Re}(\sigma_+)$ is wider than in $\mathrm{Re}(\sigma_{xx})$. Therefore,

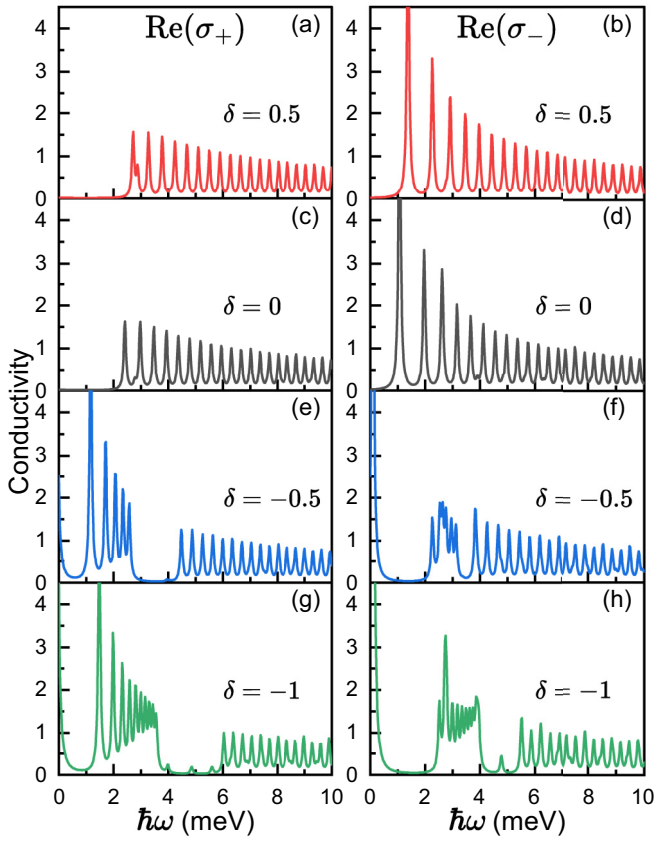


FIG. 6. The real part of right-handed polarization part magneto-optical conductivity Re($\sigma_+$) and the real part of left-handed polarization part Re($\sigma_-$) plotted for $\delta = 0.5$, 0, $-0.5$, and $-1$ meV (from top to bottom). Other parameters are taken as the magnetic field $B = 0.5$ T and the chemical potential $\mu = 0$ meV.

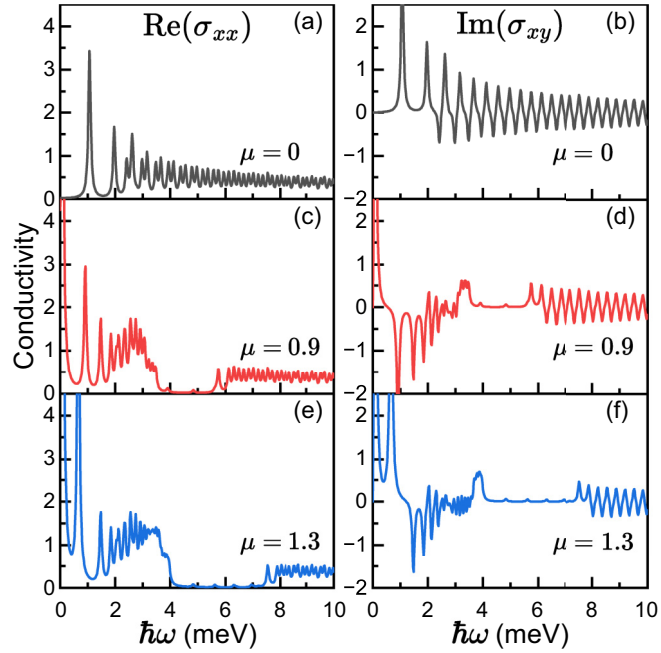


FIG. 7. The real part of longitudinal magneto-optical conductivity Re($\sigma_{xx}$) and the imaginary part of transverse Hall conductivity Im($\sigma_{xx}$) plotted for $\mu = 0$, 0.9, and 1.3 meV (from top to bottom), respectively. Other system parameters are taken as the charge transfer gap $\delta = 0$ meV and the megnetic field $B = 0.5$ T.

the signature of band inversion can be directly observed by studying the circular polarization conductance $\sigma_\pm$.

### B. Influence of chemical potential

Due to the LL transition rule, only the transitions excited from LL below the chemical potential $\mu$ to the unoccupied LL states above $\mu$, are permitted. In the subsection above, we consider the case of $\mu = 0$, where the interband transitions make the main contribution to the magneto-optical conductivity. To investigate the effect of the chemical potential $\mu$, we depict the magneto-optical conductivity as a function of $\hbar\omega$ for different values of $\mu = 0$, 0.9, and 1.3 meV in Fig. 7, where the charge transfer gap is taken as $\delta = 0$. By tuning the chemical potential, only the LL states with its energy $E_{ni} < \mu$ are occupied at low temperature and could be excited to higher unoccupied LLs, considerably modifying the LL transitions and optical absorption processes.

As illustrated in Fig. 7, the dependence of the magneto-optical conductivity on the photonic energy is not simply shifted by $\mu$ when tuning the chemical potential of the system. For different values of $\mu$, several new transitions between LLs are permitted accompanied with some transitions forbidden. As the chemical potential is tuned away from $\mu = 0$, it is shown in Fig. 7 that there is an interval region where only some small peaks are resident in. In this region, only few LL transitions are permitted, and both the magneto-optical conductance Re($\sigma_{xx}$) and Im($\sigma_{xy}$) approach small values. The appearance of the zero-conductance region is origins from the results that the transitions related to the linear-$B$-dependent LL branch are forbidden. The small peaks in this region are mainly contributed by the transitions between two $\sqrt{B}$-resolved LL branches. The energy width of the nearly-zero-conductance region increases as the chemical potential $\mu$ is tuned far from zero.

It is shown in Figs. 5 and 7 that the magneto-optical conductivity at low-frequency region indicates the similar dependence with the increase of the chemical potential $\mu$ and decrease of charge transfer gap $\delta$. A qualitative explanation for the behavior of the related peaks is that the LL transitions generate the similar effects on the peaks. As the decrease of $\delta$, the LLs spacing near the chemical potential drops and the density of states of the LL spectrum is increased. As a result, the transitions and the magneto-optical conductivity at low-frequency region are enhanced. With the increase of the chemical potential, the interband transitions are suppressed, while the intraband transitions are enhanced. Furthermore, as shown in Figs. 5 and 7, the magneto-optical conductivity in the high-frequency regime is almost unaffected when tuning the chemical potential. This could be understood as the optical transitions in the high frequency mainly relate the LLs with higher energies, where the energy difference of these transitions is rather large compared to the chemical potential modulation.

Here we start from the tight-binding model on a honeycomb lattice [52], which is used to explain the observed

quantum anomalous Hall effect in *AB*-stacked $MoTe_2/WSe_2$ moiré heterobilayers [50,51]. Differently, a tight-binding model on a triangle lattice through a detailed symmetry analysis is also proposed [64] to describe the low-energy moiré bands in this system. Although these proposed model Hamiltonians have different structures and energy bands, all of them could capture the physics of the quantum anomalous Hall effect in two-dimensional systems. The topological phase transition and band inversion are also embodied in different model Hamiltonians. In this case, some detail and quantitative values of the magneto-optical conductivity behavior are different for different lattices. However, in the low-energy regime, an extra conductance peak appears in the band-inverted case, while it is absent in the normal band case. Such a property is directly related to the physics of band inversion and can serve as a probe of the band topology. Furthermore, similar magneto-optical signatures are also indicated in several other topological systems [11,12,27].

## IV. CONCLUSION

In conclusion, we investigate the LL spectrum and the magneto-optical conductivity of a band-inverted charge transfer insulator on a honeycomb lattice based on a three-band model, which describes the low-energy physics of moiré transition metal dichalcogenide bilayer. Effects of the charge transfer gap, the magnetic field, and the chemical potential on the LLs and the transport properties are discussed in detail. It is shown that two branches of LL are $\sqrt{B}$ resolved as a function of the magnetic field $B$, while the third LL spectrum indicates the linear-$B$ dependence. With the increase of the magnetic field, two branches of $\sqrt{B}$-resolved LLs are always separated by an energy gap, while the linear-$B$-resolved LL branch crosses between the valence and conduction bands in the band-inverted case. This feature of LLs is consistent with several other topological systems, and it can be used to probe the band topology. In the low magnetic field regime, electronic states of the linear-$B$-resolved LL branch are occupied in a small energy range.

The magneto-optical conductivity is sensitive to the properties of LLs. Here the magneto-optical conductivity indicates quite different behaviors in the band-inverted case and the normal band case. It is found that the magneto-optical conductance peaks show discontinuity points when the band inversion occurs. With the increase of the magnetic field, the discontinuity point of the conductance peaks moves towards the higher photonic energy regime. The magneto-optical conductivity also manifests the closing and reopening signatures of the energy band. In the low-frequency regime, the conductance peak only appears in the band-inverted case, which is contributed by the intraband transitions of the linear-$B$-resolved LLs. However, the conductance peak in the low-frequency limit is absent for the normal band case. Therefore, it is expected that the magneto-optical conductivity could serve as a probe for the topological character of bands for a band-inverted charge transfer insulator.

## ACKNOWLEDGMENTS

This work was supported by the Natural Science Foundation of China under Grants No. 12074209 and No. 12274063 by the Natural Science Foundation of Sichuan Province (NSFSC, Grant No. 2024NSFSC0451) and Fund of the State Key Laboratory of Low-Dimensional Quantum Physics under Grant No. ZZ202402.

## APPENDIX: DERIVATION OF THE MATRIX ELEMENTS IN THE MAGNETO-OPTICAL CONDUCTIVITY

In this Appendix we present the derivation of the matrix elements in the magneto-optical conductivity. By introducing $a^\dagger = \frac{l_B}{\sqrt{2}}(\Pi_x + i\Pi_y)$, $a = \frac{l_B}{\sqrt{2}}(\Pi_x - i\Pi_y)$, we have $\Pi_x = \frac{1}{\sqrt{2}l_B}(a^\dagger + a)$, $\Pi_y = \frac{i}{\sqrt{2}l_B}(a - a^\dagger)$ and the matrix elements can be expressed as

$$\langle\Psi_{n,a}|j_x|\Psi_{m,b}\rangle = (\chi^*_{na,1}\langle n| \;\; \chi^*_{na,2}\langle n+1| \;\; \chi^*_{na,3}\langle n-1|)\begin{pmatrix} -\frac{1}{m_A}\Pi_x & \lambda & -\lambda e^{i\theta} \\ \lambda & \frac{1}{m_B}\Pi_x & 0 \\ -\lambda e^{-i\theta} & 0 & \frac{1}{m_B}\Pi_x \end{pmatrix}\begin{pmatrix} \chi_{mb,1}|m\rangle \\ \chi_{mb,2}|m+1\rangle \\ \chi_{mb,3}|m-1\rangle \end{pmatrix}, \tag{A1}$$

where $m$ and $n$ is the LL index and $a, b$ represent the three eigenenergies for a certain $n$. The above calculation can be divided into two parts and the contribution from the diagonalized part is given by

$$\begin{aligned}
&(\chi^*_{na,1}\langle n| \;\; \chi^*_{na,2}\langle n+1| \;\; \chi^*_{na,3}\langle n-1|)\begin{pmatrix} -\frac{1}{m_A}\Pi_x & 0 & 0 \\ 0 & \frac{1}{m_B}\Pi_x & 0 \\ 0 & 0 & \frac{1}{m_B}\Pi_x \end{pmatrix}\begin{pmatrix} \chi_{mb,1}|m\rangle \\ \chi_{mb,2}|m+1\rangle \\ \chi_{mb,3}|m-1\rangle \end{pmatrix} \\
&= \left(-\frac{\sqrt{m}}{\sqrt{2}l_B m_A}\chi^*_{na,1}\chi_{mb,1} + \frac{\sqrt{m+1}}{\sqrt{2}l_B m_B}\chi^*_{na,2}\chi_{mb,2} + \frac{\sqrt{m-1}}{\sqrt{2}l_B m_B}\chi^*_{na,3}\chi_{mb,3}\right)\delta_{n,m-1} \\
&+ \left(-\frac{\sqrt{m+1}}{\sqrt{2}l_B m_A}\chi^*_{na,1}\chi_{mb,1} + \frac{\sqrt{m+2}}{\sqrt{2}l_B m_B}\chi^*_{na,2}\chi_{mb,2} + \frac{\sqrt{m}}{\sqrt{2}l_B m_B}\chi^*_{na,3}\chi_{mb,3}\right)\delta_{n,m+1},
\end{aligned} \tag{A2}$$

and the second part is

$$(\chi^*_{na,1}\langle n|\chi^*_{na,2}\langle n+1|\chi^*_{na,3}\langle n-1|)\begin{pmatrix}0 & \lambda & -\lambda e^{i\theta}\\ \lambda & 0 & 0\\ -\lambda e^{-i\theta} & 0 & 0\end{pmatrix}\begin{pmatrix}\chi_{mb,1}|m\rangle\\ \chi_{mb,2}|m+1\rangle\\ \chi_{mb,3}|m-1\rangle\end{pmatrix}$$
$$=\lambda\chi^*_{na,2}\chi_{mb,1}\delta_{n,m-1}+\lambda\chi^*_{na,1}\chi_{mb,2}\delta_{n,m+1}-\lambda e^{i\theta}\chi^*_{na,3}\chi_{mb,1}\delta_{n,m+1}-\lambda e^{-i\theta}\chi^*_{na,1}\chi_{mb,3}\delta_{n,m-1}. \tag{A3}$$

Therefore, the total expression of $\langle\Psi_{n,a}|j_x|\Psi_{m,b}\rangle$ is given by

$$\langle\Psi_{n,a}|j_x|\Psi_{m,b}\rangle=\left(-\frac{\sqrt{n+1}}{\sqrt{2}l_Bm_A}\chi^*_{na,1}\chi_{mb,1}+\frac{\sqrt{n+2}}{\sqrt{2}l_Bm_B}\chi^*_{na,2}\chi_{mb,2}+\frac{\sqrt{n}}{\sqrt{2}l_Bm_B}\chi^*_{na,3}\chi_{mb,3}+\lambda\chi^*_{na,2}\chi_{mb,1}-\lambda e^{-i\theta}\chi^*_{na,1}\chi_{mb,3}\right)\delta_{n,m-1}$$
$$+\left(\frac{-\sqrt{n}}{\sqrt{2}l_Bm_A}\chi^*_{na,1}\chi_{mb,1}+\frac{\sqrt{n+1}}{\sqrt{2}l_Bm_B}\chi^*_{na,2}\chi_{mb,2}+\frac{\sqrt{n-1}}{\sqrt{2}l_Bm_B}\chi^*_{na,3}\chi_{mb,3}+\lambda\chi^*_{na,1}\chi_{mb,2}-\lambda e^{i\theta}\chi^*_{na,3}\chi_{mb,1}\right)\delta_{n-1,m}. \tag{A4}$$

The nonzero elements $M^{n,n-1}_{x,ii'}=\langle\Psi_{n,i}|j_x|\Psi_{n-1,i'}\rangle$ and $M^{n,n+1}_{x,ii'}=\langle\Psi_{n,i}|j_x|\Psi_{n+1,i'}\rangle$ are deduced as follows:

$$M^{n-1i'}_{x,ni}=\left(M^{ni}_{x,n-1i'}\right)^*=-\frac{\sqrt{n}}{\sqrt{2}l_Bm_A}\chi^*_{ni,1}\chi_{n-1i',1}+\frac{\sqrt{n+1}}{\sqrt{2}l_Bm_B}\chi^*_{ni,2}\chi_{n-1i',2}+\frac{\sqrt{n-1}}{\sqrt{2}l_Bm_B}\chi^*_{ni,3}\chi_{n-1i',3}$$
$$+\lambda\chi^*_{ni,1}\chi_{n-1i',2}-\lambda e^{i\theta}\chi^*_{ni,3}\chi_{n-1i',1}. \tag{A5}$$

In the case of the lowest LL with index $n=0$, the matrix element is nonzero only for $m=1$ and their expressions are evaluated as

$$\langle\Psi_{0,a}|j_x|\Psi_{1,b}\rangle=(\chi^*_{0a,1}\langle 0|\chi^*_{0a,2}\langle 1|0)\begin{pmatrix}-\frac{1}{m_A}\Pi_x & \lambda & -\lambda e^{i\theta}\\ \lambda & \frac{1}{m_B}\Pi_x & 0\\ -\lambda e^{-i\theta} & 0 & \frac{1}{m_B}\Pi_x\end{pmatrix}\begin{pmatrix}\chi_{1b,1}|1\rangle\\ \chi_{1b,2}|2\rangle\\ \chi_{1b,3}|0\rangle\end{pmatrix}. \tag{A6}$$

Repeating the above procedure, the nonzero elements in the case of $n=0$ are deduced as

$$\langle\Psi_0|j_x|\Psi'_1\rangle=-\frac{1}{\sqrt{2}l_Bm_A}\chi^*_{0a,1}\chi_{1b,1}+\frac{1}{l_Bm_B}\chi^*_{0a,2}\chi_{1b,2}+\lambda\chi^*_{0a,2}\chi_{1b,1}-\lambda e^{i\theta}\chi^*_{0a,1}\chi_{1b,3}. \tag{A7}$$

Similarly, for the matrix of the current operator $j_y$, the nonzero elements $M^{n,n-1}_{y,ii'}=\langle\Psi_{n,i}|j_y|\Psi_{n-1,i'}\rangle$ and $M^{n,n+1}_{y,ii'}=\langle\Psi_{n,i}|j_y|\Psi_{n+1,i'}\rangle$ are given by

$$M^{n-1i'}_{y,ni}=\left(M^{ni}_{y,n-1i'}\right)^*=\frac{i}{\sqrt{2}l_B}\left(\frac{\sqrt{n}}{m_A}\chi^*_{ni,1}\chi_{n-1i',1}-\frac{\sqrt{n+1}}{m_B}\chi^*_{ni,2}\chi_{n-1i',2}-\frac{\sqrt{n-1}}{m_B}\chi^*_{ni,3}\chi_{n-1i',3}\right)$$
$$-i\lambda\chi^*_{ni,1}\chi_{n-1i',2}+i\lambda e^{-i\theta}\chi^*_{ni,3}\chi_{n-1i',1}. \tag{A8}$$


[1] Y. Jiang, Z. Dun, S. Moon, H. Zhou, M. Koshino, D. Smirnov, and Z. Jiang, Landau quantization in coupled Weyl points: A case study of semimetal NbP, Nano Lett. **18**, 7726 (2018).

[2] Y. Hayashi, Y. Okamura, N. Kanazawa, T. Yu, T. Koretsune, R. Arita, A. Tsukazaki, M. Ichikawa, M. Kawasaki, Y. Tokura, and Y. Takahashi, Magneto-optical spectroscopy on Weyl nodes for anomalous and topological Hall effects in chiral MnGe, Nat. Commun. **12**, 5974 (2021).

[3] A. Akrap, M. Hakl, S. Tchoumakov, I. Crassee, J. Kuba, M. O. Goerbig, C. C. Homes, O. Caha, J. Novák, F. Teppe, W. Desrat, S. Koohpayeh, L. Wu, N. P. Armitage, A. Nateprov, E. Arushanov, Q. D. Gibson, R. J. Cava, D. van der Marel, B. A. Piot *et al.*, Magneto-optical signature of massless kane electrons in $Cd_3As_2$, Phys. Rev. Lett. **117**, 136401 (2016).

[4] B. Xu, Y. M. Dai, L. X. Zhao, K. Wang, R. Yang, W. Zhang, J. Y. Liu, H. Xiao, G. F. Chen, A. J. Taylor, D. A. Yarotski, R. P. Prasankumar, and X. G. Qiu, Optical spectroscopy of the Weyl semimetal TaAs, Phys. Rev. B **93**, 121110(R) (2016).

[5] P. E. C. Ashby and J. P. Carbotte, Chiral anomaly and optical absorption in Weyl semimetals, Phys. Rev. B **89**, 245121 (2014).

[6] S. Ahn, E. J. Mele, and H. Min, Optical conductivity of multi-Weyl semimetals, Phys. Rev. B **95**, 161112(R) (2017).

[7] D. Neubauer, J. P. Carbotte, A. A. Nateprov, A. Löhle, M. Dressel, and A. V. Pronin, Interband optical conductivity of the [001]-oriented Dirac semimetal $Cd_3As_2$, Phys. Rev. B **93**, 121202(R) (2016).

[8] C. J. Tabert, J. P. Carbotte, and E. J. Nicol, Optical and transport properties in three-dimensional Dirac and Weyl semimetals, Phys. Rev. B **93**, 085426 (2016).

[9] C. J. Tabert and J. P. Carbotte, Optical conductivity of Weyl semimetals and signatures of the gapped semimetal phase transition, Phys. Rev. B **93**, 085442 (2016).

[10] M. Alidoust and K. Halterman, Controllable nonreciprocal optical response and handedness-switching in magnetized spin-orbit coupled graphene, Phys. Rev. B **105**, 045409 (2022).

[11] B. Scharf, A. Matos-Abiague, I. Žutić, and J. Fabian, Probing topological transitions in HgTe/CdTe quantum wells by magneto-optical measurements, Phys. Rev. B **91**, 235433 (2015).

[12] M. Shah, M. Q. Mehmood, Y. S. Ang, M. Zubair, and Y. Massoud, Magneto-optical conductivity and giant Faraday-Kerr rotation in floquet topological insulators, Phys. Rev. B **107**, 235115 (2023).

[13] Q. Wu, J. Liu, Y. Guan, and O. V. Yazyev, Landau levels as a probe for band topology in graphene Moiré superlattices, Phys. Rev. Lett. **126**, 056401 (2021).

[14] V. P. Gusynin, S. G. Sharapov, and J. P. Carbotte, Anomalous absorption line in the magneto-optical response of graphene, Phys. Rev. Lett. **98**, 157402 (2007).

[15] P. E. C. Ashby and J. P. Carbotte, Magneto-optical conductivity of Weyl semimetals, Phys. Rev. B **87**, 245131 (2013).

[16] L. Ju, L. Wang, X. Li, S. Moon, M. Ozerov, Z. Lu, T. Taniguchi, K. Watanabe, E. Mueller, F. Zhang, D. Smirnov, F. Rana, and P. L. McEuen, Unconventional valley-dependent optical selection rules and landau level mixing in bilayer graphene, Nat. Commun. **11**, 2941 (2020).

[17] S. Yuan, R. Roldán, and M. I. Katsnelson, Landau level spectrum of *aba*- and *abc*-stacked trilayer graphene, Phys. Rev. B **84**, 125455 (2011).

[18] P. Liu, C. Cui, X.-P. Li, Z.-M. Yu, and Y. Yao, Landau level spectrum and magneto-optical conductivity in tilted Weyl semimetal, Phys. Rev. B **107**, 085146 (2023).

[19] H. Funk, A. Knorr, F. Wendler, and E. Malic, Microscopic view on landau level broadening mechanisms in graphene, Phys. Rev. B **92**, 205428 (2015).

[20] D. Wang and G. Jin, Combined effect of magnetic and electric fields on Landau level spectrum and magneto-optical absorption in bilayer graphene, Europhys. Lett. **92**, 57008 (2010).

[21] S. H. R. Sena, J. M. Pereira, F. M. Peeters, and G. A. Farias, Landau levels in asymmetric graphene trilayers, Phys. Rev. B **84**, 205448 (2011).

[22] J. M. Shao and G. W. Yang, Magneto-optical conductivity of Weyl semimetals with quadratic term in momentum, AIP Adv. **6**, 025312 (2016).

[23] J. Li, Y. Sun, M. Wu, and H. Pan, Novel electric field effects on magneto-optical conductivity in eight-pmmn borophene, J. Phys.: Condens. Matter **33**, 185501 (2021).

[24] J. D. Malcolm and E. J. Nicol, Magneto-optics of general pseudospin-s two-dimensional Dirac-Weyl fermions, Phys. Rev. B **90**, 035405 (2014).

[25] R.-L. Chu, X. Li, S. Wu, Q. Niu, W. Yao, X. Xu, and C. Zhang, Valley-splitting and valley-dependent inter-Landau-level optical transitions in monolayer $MoS_2$ quantum Hall systems, Phys. Rev. B **90**, 045427 (2014).

[26] X. Yuan, Z. Yan, C. Song, M. Zhang, Z. Li, C. Zhang, Y. Liu, W. Wang, M. Zhao, Z. Lin, T. Xie, J. Ludwig, Y. Jiang, X. Zhang, C. Shang, Z. Ye, J. Wang, F. Chen, Z. Xia, D. Smirnov *et al.*, Chiral Landau levels in Weyl semimetal nbas with multiple topological carriers, Nat. Commun. **9**, 1854 (2018).

[27] Z. Li and J. P. Carbotte, Magneto-optical conductivity in a topological insulator, Phys. Rev. B **88**, 045414 (2013).

[28] M. Calixto, N. A. Cordero, E. Romera, and O. Castaños, Signatures of topological phase transitions in higher Landau levels of HgTe/CdTe quantum Wells from an information theory perspective, Phys. A (Amsterdam) **605**, 128057 (2022).

[29] E. Illes and E. J. Nicol, Magnetic properties of the $\alpha-T_3$ model: Magneto-optical conductivity and the Hofstadter butterfly, Phys. Rev. B **94**, 125435 (2016).

[30] D. I. Khomskii, *Transition Metal Compounds* (Cambridge University Press, Cambridge, 2014).

[31] C. A. Marianetti, G. Kotliar, and G. Ceder, A first-order Mott transition in $LixCoO_2$, Nat. Mater. **3**, 627 (2004).

[32] P. A. Lee, N. Nagaosa, and X.-G. Wen, Doping a Mott insulator: Physics of high-temperature superconductivity, Rev. Mod. Phys. **78**, 17 (2006).

[33] M. Imada, A. Fujimori, and Y. Tokura, Metal-insulator transitions, Rev. Mod. Phys. **70**, 1039 (1998).

[34] Y. Tokura, Quantum materials at the crossroads of strong correlation and topology, Nat. Mater. **21**, 971 (2022).

[35] D. P. Arovas, E. Berg, S. A. Kivelson, and S. Raghu, The Hubbard model, Annu. Rev. Condens. Matter Phys. **13**, 239 (2022).

[36] W. Witczak-Krempa, G. Chen, Y. B. Kim, and L. Balents, Correlated quantum phenomena in the strong spin-orbit regime, Annu. Rev. Condens. Matter Phys. **5**, 57 (2014).

[37] J. Zaanen, G. A. Sawatzky, and J. W. Allen, The electronic structure and band gaps in transition metal compounds, J. Magn. Magn. Mater. **54-57**, 607 (1986).

[38] J. Zaanen and G. A. Sawatzky, Systematics in band gaps and optical spectra of 3D transition metal compounds, J. Solid State Chem. **88**, 8 (1990).

[39] J. Zaanen, G. A. Sawatzky, and J. W. Allen, Band gaps and electronic structure of transition-metal compounds, Phys. Rev. Lett. **55**, 418 (1985).

[40] X. Bu and Y. Li, Optical signature for distinguishing between Mott-Hubbard, intermediate, and charge-transfer insulators, Phys. Rev. B **106**, L241101 (2022).

[41] F. Wu, T. Lovorn, E. Tutuc, and A. H. MacDonald, Hubbard model physics in transition metal dichalcogenide Moiré bands, Phys. Rev. Lett. **121**, 026402 (2018).

[42] F. Wu, T. Lovorn, E. Tutuc, I. Martin, and A. H. MacDonald, Topological insulators in twisted transition metal dichalcogenide homobilayers, Phys. Rev. Lett. **122**, 086402 (2019).

[43] K. Slagle and L. Fu, Charge transfer excitations, pair density waves, and superconductivity in Moiré materials, Phys. Rev. B **102**, 235423 (2020).

[44] Y. Zhang, N. F. Q. Yuan, and L. Fu, Moiré quantum chemistry: Charge transfer in transition metal dichalcogenide superlattices, Phys. Rev. B **102**, 201115(R) (2020).

[45] E. C. Regan, D. Wang, C. Jin, M. I. Bakti Utama, B. Gao, X. Wei, S. Zhao, W. Zhao, Z. Zhang, K. Yumigeta, M. Blei, J. D. Carlström, K. Watanabe, T. Taniguchi, S. Tongay, M. Crommie, A. Zettl, and F. Wang, Mott and generalized Wigner crystal states in $WSe_2/WS_2$ moiré superlattices, Nature (London) **579**, 359 (2020).

[46] Y. Tang, L. Li, T. Li, Y. Xu, S. Liu, K. Barmak, K. Watanabe, T. Taniguchi, A. H. MacDonald, J. Shan, and K. F. Mak,

Simulation of Hubbard model physics in $WSe_2/WS_2$ moiré superlattices, Nature (London) **579**, 353 (2020).

[47] Y. Shimazaki, I. Schwartz, K. Watanabe, T. Taniguchi, M. Kroner, and A. Imamoğlu, Strongly correlated electrons and hybrid excitons in a Moiré heterostructure, Nature (London) **580**, 472 (2020).

[48] S. Shabani, D. Halbertal, W. Wu, M. Chen, S. Liu, J. Hone, W. Yao, D. N. Basov, X. Zhu, and A. N. Pasupathy, Deep Moiré potentials in twisted transition metal dichalcogenide bilayers, Nat. Phys. **17**, 720 (2021).

[49] Y. Zhang, T. Liu, and L. Fu, Electronic structures, charge transfer, and charge order in twisted transition metal dichalcogenide bilayers, Phys. Rev. B **103**, 155142 (2021).

[50] T. Li, S. Jiang, B. Shen, Y. Zhang, L. Li, Z. Tao, T. Devakul, K. Watanabe, T. Taniguchi, L. Fu, J. Shan, and K. F. Mak, Quantum anomalous Hall effect from intertwined Moiré bands, Nature (London) **600**, 641 (2021).

[51] Y. Zhang, T. Devakul, and L. Fu, Spin-textured chern bands in ab-stacked transition metal dichalcogenide bilayers, Proc. Natl. Acad. Sci. USA **118**, e2112673118 (2021).

[52] T. Devakul and L. Fu, Quantum anomalous hall effect from inverted charge transfer gap, Phys. Rev. X **12**, 021031 (2022).

[53] K. Sun, H. Yao, E. Fradkin, and S. A. Kivelson, Topological insulators and nematic phases from spontaneous symmetry breaking in 2D fermi systems with a quadratic band crossing, Phys. Rev. Lett. **103**, 046811 (2009).

[54] K. Sun, W. V. Liu, A. Hemmerich, and S. Das Sarma, Topological semimetal in a fermionic optical lattice, Nat. Phys. **8**, 67 (2012).

[55] Z. Zhu, Y. Cheng, and U. Schwingenschlögl, Band inversion mechanism in topological insulators: A guideline for materials design, Phys. Rev. B **85**, 235401 (2012).

[56] C.-X. Liu, S.-C. Zhang, and X.-L. Qi, The quantum anomalous Hall effect: Theory and experiment, Annu. Rev. Condens. Matter Phys. **7**, 301 (2016).

[57] C.-Z. Chang, C.-X. Liu, and A. H. MacDonald, *Colloquium*: Quantum anomalous Hall effect, Rev. Mod. Phys. **95**, 011002 (2023).

[58] P. Olalde-Velasco, J. Jiménez-Mier, J. D. Denlinger, Z. Hussain, and W. L. Yang, Direct probe of Mott-Hubbard to charge-transfer insulator transition and electronic structure evolution in transition-metal systems, Phys. Rev. B **83**, 241102(R) (2011).

[59] J. R. Meyer, R. J. Wagner, F. J. Bartoli, C. A. Hoffman, M. Dobrowolska, T. Wojtowicz, J. K. Furdyna, and L. R. Ram-Mohan, Magneto-optical properties of HgTe-CdTe superlattices, Phys. Rev. B **42**, 9050 (1990).

[60] B. Scharf, A. Matos-Abiague, and J. Fabian, Magnetic properties of HgTe quantum Wells, Phys. Rev. B **86**, 075418 (2012).

[61] M. Schultz, U. Merkt, A. Sonntag, U. Rössler, R. Winkler, T. Colin, P. Helgesen, T. Skauli, and S. Løvold, Crossing of conduction- and valence-subband Landau levels in an inverted HgTe/CdTe quantum Well, Phys. Rev. B **57**, 14772 (1998).

[62] G. D. Mahan, *Many-Particle Physics* (Springer, New York, 2000).

[63] T. Ando and Y. Uemura, Theory of quantum transport in a two-dimensional electron system under magnetic fields. I. Characteristics of level broadening and transport under strong fields, J. Phys. Soc. Jpn. **36**, 959 (1974).

[64] X.-J. Luo, M. Wang, and F. Wu, Symmetric wannier states and tight-binding model for quantum spin hall bands in *AB*-stacked $MoTe_2/WSe_2$, Phys. Rev. B **107**, 235127 (2023).